





Discrete symmetries control geometric mechanics in parallelogram-based origami

James McInerney^{a,b,1} , Glaucio H. Paulino^{c,d,e,f}, and D. Zeb Rocklin^{a,1} 

Edited by Shu Yang, University of Pennsylvania, Philadelphia, PA; received February 15, 2022; accepted June 20, 2022 by Editorial Board Member Yonggang Huang

Geometric compatibility constraints dictate the mechanical response of soft systems that can be utilized for the design of mechanical metamaterials such as the negative Poisson's ratio Miura-ori origami crease pattern. Here, we develop a formalism for linear compatibility that enables explicit investigation of the interplay between geometric symmetries and functionality in origami crease patterns. We apply this formalism to a particular class of periodic crease patterns with unit cells composed of four arbitrary parallelogram faces and establish that their mechanical response is characterized by an anticommuting symmetry. In particular, we show that the modes are eigenstates of this symmetry operator and that these modes are simultaneously diagonalizable with the symmetric strain operator and the antisymmetric curvature operator. This feature reveals that the anticommuting symmetry defines an equivalence class of crease pattern geometries that possess equal and opposite in-plane and out-of-plane Poisson's ratios. Finally, we show that such Poisson's ratios generically change sign as the crease pattern rigidly folds between degenerate ground states and we determine subfamilies that possess strictly negative in-plane or out-of-plane Poisson's ratios throughout all configurations.

origami | symmetry | metamaterials

Discrete symmetries characterize the properties of physical systems (1, 2) ranging from topological insulators and superconductors (3–6) to frustrated magnets (7) and mechanical metamaterials (8). Such symmetries can dictate the rigid deformations of periodic mechanical networks (9), including the generation of negative Poisson's ratio (auxetic) modes (10, 11). Such auxetic mechanical metamaterials are characterized by either dilational strain or synclastic (dome-like) curvature and are desirable for a variety of applications in engineering that may not be achieved with conventional materials (12–15). While this dilational in-plane behavior of auxetic materials typically couples to synclastic out-of-plane behavior (16), a family of highly symmetric origami crease patterns exhibits equal and opposite in-plane and out-of-plane Poisson's ratios (17–20).

Origami structures and assemblies are composed of thin sheets whose low-energy mechanical response is dictated by the geometry of their crease patterns (21–24) via compatibility conditions that restrict deformations to isometries that transform the sheets without stretching their faces (25, 26). Modern fabrication and actuation techniques can be used to self-fold such structures at the macroscale (27–29) as well as at the nano- and microscales (30–38) for applications in engineering (39, 40) and soft robotics (41–44). These isometric configurations can be considered as degenerate ground states that rely on symmetries of the crease pattern to rigidly fold (45–49); however, interplay between these symmetries and the functionality of origami as mechanical metamaterials (50) with negative Poisson's ratios (17–20) or high stiffness-to-weight ratios (51) has not been explored explicitly.

The linear isometries of an infinitesimally thin origami sheet are conventionally modeled via the rigid deformations of its triangulation (52, 53), where “virtual” creases are introduced to accommodate bending (without stretching) of the faces. Such rigid deformations can be specified either via vertex displacements that do not stretch any physical or virtual creases (54) (as commonly applied to mechanical networks composed of point masses and central-force springs) or via folding about the creases that does not rotate elements of the sheet relative to themselves (55, 56). This latter approach has been applied to the Morph family of parallelogram-based crease patterns (20), expanding upon previous investigations of the Miura-ori (17, 18) and eggbox (19) crease patterns, thereby showing both analytically and numerically the existence of equal and opposite in-plane and out-of-plane Poisson's ratios. While it is straightforward to show numerically that this result holds for the crease patterns with more generic parallelogram faces discussed herein, analytical solutions become intractable in the absence of multiple symmetries that obfuscate the underlying physical principle.

Significance

Origami-inspired metamaterials utilize crease geometries, often based on symmetries, to generate deployable and reconfigurable structures with unusual properties such as negative Poisson's ratios and high stiffness-to-weight ratios. Mathematical treatments of such structures are often complex and ad hoc, thereby preventing far-reaching analytical solutions and obscuring the interplay between geometry and mechanical response. Here, we present a unifying analytical framework for the low-energy deformations (linear isometries) of quadrilateral-based origami, including mechanical metamaterials currently under intense study, that highlights the role of symmetry in a broad family of crease patterns exhibiting equal and opposite in-plane and out-of-plane Poisson's ratios. This approach extends to nonuniform deformations and to other crease patterns where symmetry plays a fundamental role in the material properties.

Author contributions: J.M., G.H.P., and D.Z.R. designed research; J.M. and D.Z.R. performed research; and J.M., G.H.P., and D.Z.R. wrote the paper.

The authors declare no competing interest.

This article is a PNAS Direct Submission. S.Y. is a guest editor invited by the Editorial Board.

Copyright © 2022 the Author(s). Published by PNAS. This article is distributed under [Creative Commons Attribution-NonCommercial-NoDerivatives License 4.0 \(CC BY-NC-ND\)](https://creativecommons.org/licenses/by-nc-nd/4.0/).

¹To whom correspondence may be addressed. Email: jmcinern@umich.edu or zebrocklin@gatech.edu.

This article contains supporting information online at <https://www.pnas.org/lookup/suppl/doi:10.1073/pnas.2202777119/-DCSupplemental>.

Published August 3, 2022.

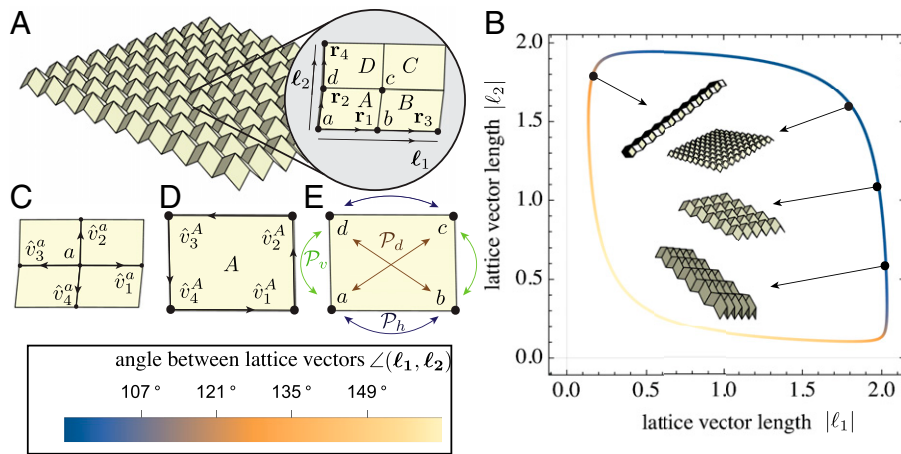


Fig. 1. (A) An example four-parallel-gram origami tessellation and its unit cell characterized by the four edge vectors (specified up to overall scaling), \mathbf{r}_1 , \mathbf{r}_2 , \mathbf{r}_3 , and \mathbf{r}_4 , that specify the two generically nonorthogonal lattice vectors, $\ell_1 = \mathbf{r}_1 + \mathbf{r}_3$ and $\ell_2 = \mathbf{r}_2 + \mathbf{r}_4$. (B) Degenerate ground states of the four-parallel-gram origami shown in A where the color indicates the angle between the lattice vectors. (C and D) Local notation for edges at the (C) vertex and (D) face specified by the superscript, where the subscript specifies the local edge index that increases cyclically in counterclockwise order. (E) Labeling of the vertices in the unit cell under various two-cycle permutations, \mathcal{P}_h , \mathcal{P}_v , and \mathcal{P}_d , each satisfying $\mathcal{P}^2 = 1$.

In this work, we introduce an alternative model for the linear isometries of parallelogram-based origami that yields elegant analytic formulas for the in-plane and out-of-plane Poisson's ratios and elucidates their equal and opposite relationship, for the unexplored periodic crease patterns with unit cells composed of four arbitrary parallelogram faces. We first introduce this family of four-parallel-gram origami that generalizes the Miura-ori (17, 18), the eggbox (19), and the Morph crease patterns (20). We then derive compatibility constraints for the linear isometries and show that they possess an anticommuting symmetry that constrains the linear isometries at both the intracellular and intercellular scales. This leads us to our key result that the system has a symmetric linear isometry with an in-plane Poisson's ratio that is equal and opposite to the out-of-plane Poisson's ratio for the system's antisymmetric linear isometry, implying that one is always negative. Finally, we explore how these Poisson's ratios may change sign as the crease pattern rigidly folds along its one-dimensional configuration space of degenerate ground states. We close with concluding remarks that address extension to future work and experimental implementation.

Results and Discussion

Four-Parallel-gram Origami. Investigations of origami sheets typically rely on highly symmetric crease patterns, such as the renowned Miura-ori, to simplify the analysis. Here, we introduce the completely generic family of four-parallel-gram origami and discuss the sole symmetry that governs its members' linear response, including the special cases of the Miura-ori (17, 18), the eggbox (19), and the Morph (20). We provide further details on the design space of such crease patterns in *SI Appendix, section 1A*.

Consider spatially periodic origami sheets composed of cells with four arbitrary parallelogram faces such as that shown in Fig. 1A, *Inset*. These cells are defined by the four unique edge vectors, \mathbf{r}_i , and their vertices are generically nondevelopable, which means that they cannot necessarily be folded from a single sheet of material. Note that only the relative length of these edges matters as the geometric mechanics studied herein are independent of overall scale. In contrast to the aforementioned special cases, the lattice vectors, $\ell_1 = \mathbf{r}_1 + \mathbf{r}_3$ and $\ell_2 = \mathbf{r}_2 + \mathbf{r}_4$, are generically nonorthotropic, $\ell_1 \cdot \ell_2 \neq 0$; moreover, the lattice vectors stretch

and shear along the one-dimensional manifold of degenerate ground states (*SI Appendix, section 1B*) such as those shown in Fig. 1B. Since periodic origami composed of arbitrary quadrilateral faces cannot be rigidly folded (57), these crease patterns must possess a symmetry that renders its constraints redundant (49), which can be characterized by introducing local notation for the edges.

Because our analysis involves detailed examination of individual vertices, in addition to the globally defined edge vectors, \mathbf{r}_i , we now introduce the local edge vectors, \mathbf{v}_i^a , of vertex a , where i cyclically labels the edges in counterclockwise order as shown in Fig. 1C. For either of the two pairs of nonadjacent vertices in the unit cell, the same edges that emanate from one enter the other. Consequently, the locally defined edges are antisymmetric under the permutation operation $\mathcal{P}_d = \mathcal{P}_h \mathcal{P}_v = \mathcal{P}_v \mathcal{P}_h$ introduced in Fig. 1E that swaps nonadjacent vertices: $\mathbf{v}_i^{\mathcal{P}_d a} = -\mathbf{v}_{i+2}^a$. Note that these permutations are two cycles, $\mathcal{P}^2 = 1$, and are isomorphic to the twofold rotoinversion spatial symmetry of the crease pattern. In this way, the permutation symmetries that we consider are analogous to conventional spatial symmetries, but they are instead combinatorial, with less reliance on the spatial configuration of the unit cell.

Similarly, let \mathbf{v}_i^A denote the edges bounding a face where A labels the face and i cyclically labels the edge in counterclockwise order as shown in Fig. 1D. Since the faces are all parallelograms, every other edge is antiparallel, $\mathbf{v}_{i+2}^A = -\mathbf{v}_i^A$. Consequently, the interior (sector) angles of the face are supplementary at adjacent vertices and identical at nonadjacent vertices. In contrast to the vertex symmetry of the four-parallel-gram, this feature holds for crease patterns with arbitrary numbers of parallelogram faces, which has implications for the isometries discussed in the next section.

Linear Isometries and Compatibility Conditions. The low-energy response of origami sheets is dominated by linear isometries that rotate elements of the sheet without stretching them. Such rotations include both folding at the creases and bending of the faces, which are treated equivalently in previous works (17–20). Here, we derive compatibility conditions that distinguish between these two types of local isometries and show that the linear isometries of parallelogram-based origami are governed by a compatibility matrix that exclusively depends on vertex folding.

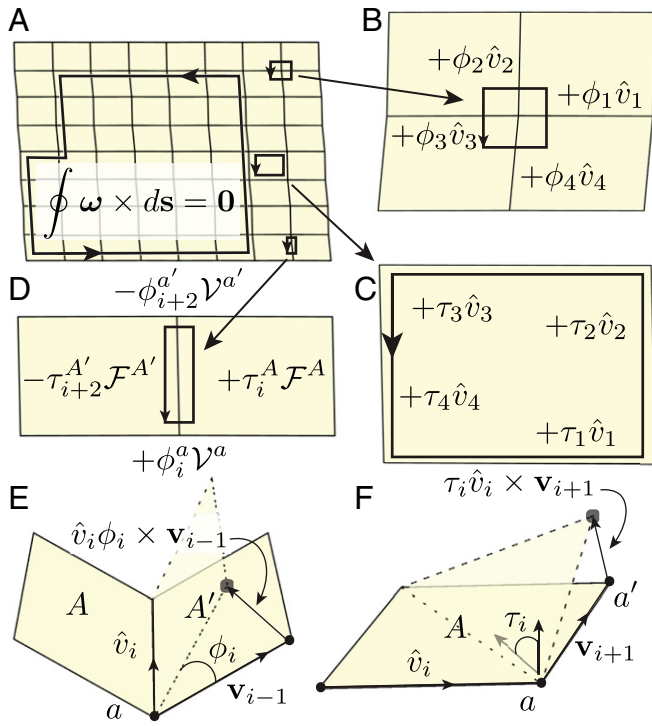


Fig. 2. Compatibility conditions for linear isometries. (A) The loop integral of the angular velocity must vanish over arbitrary closed paths. (B) Folding about crease i in the vicinity of vertex a induces a rotation generated by $\phi_i^a \hat{v}_i^a$ that accumulates along subsequent creases and must vanish over a closed path as dictated by Eq. 4. (C) Applying a torsion along crease i on face A induces a rotation generated by $\tau_i^A \hat{v}_i^A$ (indicated by the change in the normal of the face in bottom right corner) as well as a displacement $\tau_i^A \hat{v}_i^A \times \mathbf{v}_{i+1}^A$ that accumulates along subsequent creases and must vanish over a closed path as dictated by Eq. 5. (D) The vertex folds and face torsions couple via compatibility in Eq. 6. (E and F) Schematic of (E) vertex folding and (F) face bending along with the displacements these rotations generate.

The linear isometries are described by a spatially varying, temporally static angular velocity field, $\omega(x_1, x_2)$, defined over the continuous surface coordinates (x_1, x_2) , that rotates infinitesimal vectors of the sheet, $d\mathbf{X}$, relative to one another. Since these rotations must preserve the length of any closed loop on the surface of the sheet (such as that shown in Fig. 2A), the angular velocity is constrained by the compatibility condition

$$\oint \omega \times d\mathbf{X} = 0. \quad [1]$$

Application of Stokes' theorem to Eq. 1 over a single face shows that the angular velocity gradients must lie in the plane of the face to satisfy $\partial_1 \omega_3 = \partial_2 \omega_3 = 0$, where x_3 is a coordinate locally orthogonal to the surface, and hence must point along the edges at the boundary to match with the adjacent faces. Thus, the interior of the face can undergo any linear isometry of a plane provided that the angular velocity is compatible between different corners of the sheet.

Such corners, including those that the paths shown in Fig. 2 A–D pass through, can be labeled by the vertex (denoted via lowercase Latin indexes) and face (denoted via uppercase Latin indexes) that they are adjacent to. Any two corners of the origami sheet, (a, A) and (a', A') , are connected via a sequence of paths across and along creases, such as a portion of the closed loop in Fig. 2A. Since gradients in the angular velocity must lie in the plane of each face, they must be parallel to the edges near the intersection of two faces. Thus, the angular velocity gradient between the corners of two edge-sharing faces,

$\omega^{(a, A')} - \omega^{(a, A)} = \pm \phi_i^a \hat{v}_i^a$, corresponds to applying a fold, ϕ , over the crease i (Fig. 2E) while similarly, the angular velocity gradient between the corners of two vertices that share both a face and an edge, $\omega^{(a', A)} - \omega^{(a, A)} = \pm \tau_i^A \hat{v}_i^A$, corresponds to applying a torsion, τ , along the crease i (Fig. 2F). By convention, the sign is positive (negative) when the crease is traversed along (against) the ordering of the local edges in both cases.

The angular velocity gradients and the vertex displacements, \mathbf{u}_i , that they generate accumulate along the path between the two corners:

$$\omega^{(a, A)} - \omega^{(a_0, A_0)} = \sum_{i', a'} \pm \phi_{i'}^{a'} \hat{v}_{i'}^{a'} + \sum_{i', A'} \pm \tau_{i'}^{A'} \hat{v}_{i'}^{A'}, \quad [2]$$

$$\mathbf{u}^{(a, A)} - \mathbf{u}^{(a_0, A_0)} = \sum_{i', a', A'} \omega^{(a', A')} \times \mathbf{v}_{i'}^{a'}. \quad [3]$$

Note that since the vertex displacements contain a double summation in Eq. 3, they grow quadratically between cells, implying that the angular velocity field generically induces some amount of intercellular curvature. These folds and torsions must satisfy the compatibility condition in Eq. 1 over any closed sequence of corners. Such a sequence constrains the folds in the vicinity of a vertex, as illustrated in Fig. 2B, and the torsions on the boundary of a face, as illustrated in Fig. 2C, while the edges couple the folds to the torsions as illustrated in Fig. 2D:

$$\sum_{i'} \phi_{i'}^a \hat{v}_{i'}^a = 0, \quad [4]$$

$$\sum_{i'} \tau_{i'}^A \hat{v}_{i'}^A = 0, \quad \tau_i^A \hat{v}_i^A \times \mathbf{v}_{i+1}^A = \tau_{i-1}^A \hat{v}_{i-1}^A \times \mathbf{v}_{i-2}^A, \quad [5]$$

$$\phi_i^a + \tau_j^A - \phi_{i+2}^a - \tau_{j+2}^A = 0. \quad [6]$$

The vertex condition is the familiar result in the literature (55, 56), which is the linearization of the Belcastro–Hull vertex condition (26), but importantly, it holds to linear order even as the faces are bending. Similarly, the face-bending condition is independent of the folding about the adjacent vertices. However, these folding and bending motions become coupled via the edge constraint, which is now nontrivial because different changes in orientation occur as one passes across the edge at two different vertices and along it at two different faces. Importantly, the vertex and face compatibility conditions in Eqs. 4 and 5 respectively admit one-dimensional analytical solutions. Note that for triangular faces, these face compatibility conditions admit only trivial solutions so that the isometries are restricted to vertex folding.

Projecting the cross-product of the directions of any two edges emanating from the vertex, $\hat{v}_i^a \times \hat{v}_j^a$, onto Eq. 4 reveals that the vertex folds are proportional to triple products of edge directions, $\zeta_i^a \equiv \hat{v}_{i+1}^a \cdot \hat{v}_{i+2}^a \times \hat{v}_{i+3}^a$, where ζ_i is defined modulo 4. For parallelogram faces, $\mathbf{v}_i^A = -\mathbf{v}_{i+2}^A$, the torsions must be proportional to their edge lengths to satisfy Eq. 5. These proportionality factors are, respectively, the vertex amplitudes, \mathcal{V}^a , and the face amplitudes, \mathcal{F}^A , that determine the local solutions:

$$\phi_i^a = (-1)^i \mathcal{V}^a \zeta_i^a, \quad [7]$$

$$\tau_i^A = (-1)^i \mathcal{F}^A v_i^A. \quad [8]$$

Note that while the vertex amplitudes have no units, the face amplitudes must have units of inverse length to ensure that the angular velocity is dimensionless. The physical significance of these amplitudes is discussed in *SI Appendix, section 2A*.

That the folding and torsions take the forms in Eqs. 7 and 8 is a necessary and sufficient condition that the deformation is compatible in loops around vertices (Fig. 2B) and faces (Fig. 2C), respectively. Substitution of the local solutions from Eqs. 7 and 8 into the edge compatibility condition, Eq. 6, yields

$$\mathcal{V}^a \zeta_i^a - \mathcal{V}^{a'} \zeta_{i+2}^{a'} + (\mathcal{F}^A - \mathcal{F}^{A'}) v_i^a = 0. \quad [9]$$

One consequence of this constraint is that there is always an isometry consisting of uniform face deformations, $\mathcal{F}^A = \mathcal{F}^{A'}$, and vanishing vertex amplitudes $\mathcal{V}^A = 0$. Up to this isometry, the solutions of Eq. 9 are equivalent to those formed by combining the four edge constraints (divided by their respective edge lengths) to arrive at a compatibility constraint associated with vertex i expressed purely in terms of its amplitude and the amplitudes of the four neighboring vertices:

$$\sum_{i'} \left(\frac{\zeta_{i'}^a}{v_{i'}^a} \mathcal{V}^a - \frac{\zeta_{i'+2}^{a'}}{v_{i'+2}^{a'}} \mathcal{V}^{a'} \right) = 0. \quad [10]$$

The amplitudes that satisfy Eq. 10 at every vertex are linear isometries whose corresponding face amplitudes are determined by inverting the edge compatibility condition in Eq. 9 (SI Appendix, section 1). These isometries are equivalent to those modeled by a triangulation; hence, there are generically two such modes in addition to the uniform face-bending mode (57). These constraints can be concatenated to compose the compatibility matrix, \mathbf{C} , that maps the vertex amplitudes, $|\mathcal{V}\rangle$, to the constraint in Eq. 10 at every vertex so that the linear isometries span the matrix's nullspace $\mathbf{C}|\mathcal{V}\rangle = \mathbf{0}$. In this notation, the "bra," $\langle \mathcal{V}_1|$, and "ket," $|\mathcal{V}_2\rangle$, have the inner product $\langle \mathcal{V}_1|\mathcal{V}_2\rangle = \mathbf{V}_1^\dagger \cdot \mathbf{V}_2$, where \dagger denotes complex conjugation, and transform under matrix operators as $\langle \mathcal{V}|\mathbf{C} = \langle \mathbf{C}\mathcal{V}|$ and $\mathbf{C}|\mathcal{V}\rangle = |\mathbf{C}\mathcal{V}\rangle$, respectively.

The uniform face-bending mode, $|\mathcal{V}\rangle = \mathbf{0}$, satisfying edge compatibility in Eq. 9 with uniform face amplitudes is a nontrivial linear isometry that exists for crease patterns with any number of parallelogram faces; hence, the compatibility condition in Eq. 10 is also valid for any parallelogram-based origami crease pattern. However, this is not true for generic quadrilateral faces because the face torsions in Eq. 8 no longer satisfy the face compatibility conditions in Eq. 5.

Vertex Permutation Symmetry in the Four-Parallelogram. The spatial symmetry of four-parallelogram origami constrains the linear isometries that satisfy the compatibility conditions in Eq. 10. While such modes generically vary between cells according to Bloch's theorem (54, 57), we show here that the remaining two uniform folding isometries (in addition to the pure-face isometry) are eigenstates of the permutation operator, \mathcal{P}_d , with opposite eigenvalues. Our analysis is simplified by our self-adjoint compatibility matrix that anticommutes with the permutation operator. This feature contrasts with previous work where the compatibility matrix maps between vector spaces such as vertex displacements to bond extensions (54) that transform differently under symmetries of the sheet.

The antisymmetry of the local edge vectors, $\mathbf{v}^{\mathcal{P}a} = -\mathbf{v}_{i+2}^a$, implies that the local folding coefficients are antisymmetric between nonadjacent vertices, $\zeta_i^{\mathcal{P}a} = -\zeta_{i+2}^a$. Hence, the compatibility matrix constructed from Eq. 10 anticommutes with the permutation operator:

$$\mathcal{P}_d \mathbf{C} \mathcal{P}_d = -\mathbf{C}. \quad [11]$$

The eigenbasis of this permutation is represented by the basis vectors $|\pm\pm\rangle$, where the first (second) sign indicates the eigenvalue of the basis vector under the horizontal (vertical) permutation $\mathcal{P}_{h(v)}$ illustrated in Fig. 1E:

$$\begin{aligned} |++\rangle &= \frac{1}{2} (+1 \quad +1 \quad +1 \quad +1), \\ |--\rangle &= \frac{1}{2} (+1 \quad -1 \quad +1 \quad -1), \\ |+-\rangle &= \frac{1}{2} (+1 \quad +1 \quad -1 \quad -1), \\ |-+\rangle &= \frac{1}{2} (+1 \quad -1 \quad -1 \quad +1). \end{aligned} \quad [12]$$

Importantly, the basis states $|++\rangle$ and $|--\rangle$ have eigenvalue +1 under \mathcal{P}_d while the basis states $|+-\rangle$ and $|-+\rangle$ have eigenvalue -1 under \mathcal{P}_d . Hence, the vertex amplitudes, $|\mathcal{V}\rangle = (\mathcal{V}^a \quad \mathcal{V}^b \quad \mathcal{V}^c \quad \mathcal{V}^d)$, are divided into sectors that are (anti)symmetric under such permutations, $\mathcal{P}_d |\mathcal{V}_\pm\rangle = \pm |\mathcal{V}_\pm\rangle$. Substitution of the identity, $\mathbf{1} = \mathcal{P}_d \mathcal{P}_d$, into the inner product, $\langle \mathcal{V}_\pm|\mathbf{C}|\mathcal{V}_\pm\rangle = \langle \pm\mathcal{V}_\pm|\mathcal{P}_d \mathbf{C} \mathcal{P}_d|\pm\mathcal{V}_\pm\rangle$, shows that this inner product is equal to its own opposite and hence, it must vanish. Thus, the (anti)symmetric modes automatically satisfy (anti)symmetric constraints.

Indeed, the compatibility matrix constructed from Eq. 10 is off-block diagonal (SI Appendix, section 2) in the basis from Eq. 12:

$$\mathbf{C}^{\text{sym}} = \begin{pmatrix} 0 & 0 & 0 & 0 \\ 0 & 0 & \chi_{24}^- & \chi_{13}^- \\ 0 & \chi_{24}^- & 0 & 0 \\ 0 & \chi_{13}^- & 0 & 0 \end{pmatrix}, \quad [13]$$

$$\chi_i \equiv \frac{\hat{\mathbf{r}}_{i+1} \cdot \hat{\mathbf{r}}_{i+2} \times \hat{\mathbf{r}}_{i+3}}{r_i} \equiv \frac{\mathbf{r}_{i+1} \cdot \mathbf{r}_{i+2} \times \mathbf{r}_{i+3}}{R}, \quad [14]$$

where the χ_i and χ_j are global folding coefficients, $\chi_{ij}^- \equiv \chi_j - \chi_i$ is their difference, and $R \equiv r_1 r_2 r_3 r_4$ is the product of the four unique edge lengths. In this form, the symmetric and antisymmetric modes in the nullspace are apparent,

$$|\mathcal{V}_+\rangle = |++\rangle, \quad [15]$$

$$|\mathcal{V}_-\rangle = \chi_{13}^- |+-\rangle - \chi_{24}^- |-+\rangle, \quad [16]$$

and the corresponding face amplitudes are determined explicitly in SI Appendix, section 2B, and the mapping from these amplitudes to the rigid folding of the triangulation is presented in SI Appendix, section 2C. In fact, the symmetric mode in Eq. 15 is the rigid folding motion that generates the degenerate ground states shown in Fig. 1B. The modes in Eqs. 15 and 16 along with the pure face-bending mode with uniform face amplitudes, $|\mathcal{F}\rangle = \mathbf{1}$, and vanishing vertex amplitudes, $|\mathcal{V}\rangle = \mathbf{0}$, span the three-dimensional space of linear isometries for four-parallelogram origami. The connection between these amplitudes and the description of these modes via the rigid folding of a triangulation of the origami sheet are discussed in SI Appendix, section 2C.

Strain and Curvature. Linear isometries stretch and rotate the lattice vectors that are respectively captured via the strain of the cell and the curvature between cells. Here, we derive these quantities for four-parallelogram origami as linear combinations of the vertex amplitudes and show that they have opposite eigenvalues under the permutation operator \mathcal{P}_d . We then show that this decouples the in-plane and out-of-plane modes and ensures that the corresponding Poisson's ratios are equal and opposite.

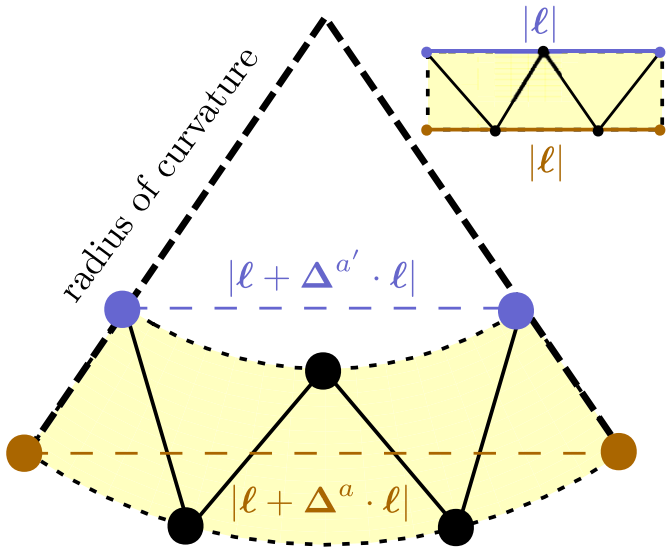


Fig. 3. An illustration of the slab-like behavior of corrugated origami sheets. Bending motions extend/compress the lattice vectors, $\Delta \cdot \ell$, by different amounts depending on which vertex, a , they are measured from so that the radius of curvature induced by a linear isometry is proportional to gradients in the lattice vectors stretches.

As measured at corner (a, A) , the lattice vector deforms according to Eq. 3 as $\Delta_{\mu}^{(a,A)} \equiv \mathbf{u}^{(a,A)}(n_{\mu} = 1) - \mathbf{u}^{(a,A)}(n_{\mu} = 0)$, where $\mu = 1$ or 2 labels the lattice direction and n_{μ} labels the cell index. The angular velocities are inherently linear in the global folding coefficients, χ_i , and the change in length introduces additional triple products of the edge vectors so that it must be quadratic in the global folding coefficients. Conveniently, the torsion displaces the lattice vector along $\mathbf{v}_i^A \times \mathbf{v}_i^{A'}$ and the additional folding between the corners of a single vertex displaces the lattice vector along $\hat{v}_i^a \times \ell_{\mu}$, which both vanish when projected onto the original lattice vector, $\ell_{\mu} = \mathbf{v}_i^A + \mathbf{v}_i^{A'}$ (SI Appendix, section 3). Thus, the lattice vector stretches locally depend only on the vertex amplitudes:

$$\ell_1 \cdot \Delta_1^{(a,A)} = \chi_2 \chi_4 R \langle a | \mathcal{P}_h | \mathcal{V} \rangle, \quad [17]$$

$$\ell_2 \cdot \Delta_2^{(a,A)} = -\chi_1 \chi_3 R \langle a | \mathcal{P}_v | \mathcal{V} \rangle, \quad [18]$$

where the bra $\langle a |$ is the original basis vector, $\langle a | \mathcal{V} \rangle = \mathcal{V}^a$, for the vertex the stretch is measured at.

While origami are intrinsically sheets, their corrugation implies that they deform as an elastic slab: upward bending extends the bottom, contracts the top, and preserves lengths in the midplane as illustrated in Fig. 3. This intuition explains the vertex dependence on the lattice vector stretches in Eqs. 17 and 18 as an analog of the height dependence on the strain of the slab. Thus, the strain of the origami sheet can be specified via that of its midplane by averaging the lattice vector stretches over its $N_v = 4$ vertices:

$$\epsilon_{\mu\mu} \equiv \frac{\ell_{\mu} \cdot \left(\sum_{a'} \Delta_{\mu}^{a'} \right)}{N_v} \equiv \langle \epsilon_{\mu\mu} | \mathcal{V} \rangle. \quad [19]$$

Note that these strains have units of area because the surface coordinates are the dimensionless cell indexes and that the subscripts denote the lattice directions without implied summation.

This same connection to elastic slabs suggests that the curvature of the sheet can also be characterized by the vertex dependence of the lattice vector stretches. The lattice vectors are rotated between cells by the corner-independent lattice angular velocity,

$\Omega_{\mu} \equiv \omega^{(a,A)}(n_{\mu} = 1) - \omega^{(a,A)}(n_{\mu} = 0)$, which lies in the plane of the sheet with normal vector $\mathbf{N} = \ell_1 \times \ell_2$ to satisfy the compatibility condition in Eq. 1. Compatibility of the vertex displacements in Eq. 3 shows that changes to the lattice vectors vary between two corners, $\Delta_{\mu}^{(a,A)} - \Delta_{\mu}^{(a',A')}$, due to the lattice rotation of the vector between the two vertices, $\Omega_{\mu} \times (\mathbf{r}_{a'} - \mathbf{r}_a)$ (where \mathbf{r}_a denotes the position of vertex a), and due to the rotation of the lattice vector by the angular velocity gradient between the two corners, $(\omega^{(a',A')} - \omega^{(a,A)}) \times \ell_{\mu}$ (SI Appendix, section 3). The latter vanishes under projection onto the initial lattice vector while the former rearranges to define the curvature, $\kappa_{\mu\mu} = \Omega_{\mu} \times \ell_{\mu} \cdot \mathbf{N}$, via differences in the lattice vector stretches:

$$\kappa_{\mu\mu} = -\frac{\ell_{\mu} \cdot (\Delta_{\mu}^{a'} - \Delta_{\mu}^a)}{(\mathbf{r}_{a'} - \mathbf{r}_a) \cdot \mathbf{N}} \equiv \langle \kappa_{\mu\mu} | \mathcal{V} \rangle. \quad [20]$$

Note that these curvatures are vertex independent and have units of inverse length because the normal vector has units of area.

In this form, both the lattice strains and the lattice curvatures depend explicitly on the locally computed lattice vector stretches. However, these operators have opposite eigenvalues under permutations of the nonadjacent vertices,

$$\mathcal{P}_d |\epsilon_{\mu\mu}\rangle = +|\epsilon_{\mu\mu}\rangle, \quad [21]$$

$$\mathcal{P}_d |\kappa_{\mu\mu}\rangle = -|\kappa_{\mu\mu}\rangle; \quad [22]$$

hence, they couple to opposite sectors of linear isometries. In fact, since each sector contains exactly one mode, the in-plane strains are exclusively generated by the symmetric mode, $|\mathcal{V}_+\rangle$, and the out-of-plane curvatures are exclusively generated by the antisymmetric mode, $|\mathcal{V}_-\rangle$, which are orthogonal to one another. Thus, the fundamental symmetries explain why these structures have one mode that generates only in-plane strain and one mode that generates only out-of-plane bending, as observed for the planar and bend modes of previous work (17, 18, 20).

Finally, the relative strain and curvature in transverse lattice directions define geometric Poisson's ratios:

$$\nu_{\text{in}} \equiv -\frac{|\ell_2|^2 \epsilon_{11}}{|\ell_1|^2 \epsilon_{22}}, \quad [23]$$

$$\nu_{\text{out}} \equiv -\frac{|\ell_2|^2 \kappa_{11}}{|\ell_1|^2 \kappa_{22}}. \quad [24]$$

Such ratios depend entirely on the triple products entering the lattice vector stretches with the exception that the antisymmetry of the lattice curvature operators leads to opposite signs in the numerator and denominator while the symmetry of the lattice strain operators leads to the same signs. Thus, the Poisson's ratios are always equal and opposite:

$$\nu_{\text{in}} = -\nu_{\text{out}} = \frac{|\ell_2|^2 \chi_2 \chi_4}{|\ell_1|^2 \chi_1 \chi_3}. \quad [25]$$

Note that this Poisson's ratio is a purely geometric quantity and it can increase and decrease without limit because the lattice is not isotropic (58). Furthermore, recall that generic four-parallel-gram origami sheets are not orthotropic so that their Poisson's ratios are not necessarily equal and opposite as measured from orthogonal directions. As shown in SI Appendix, section 3D, this recovers the result for the Morph subfamily of four-parallel-gram origami from ref. 20.

The off-diagonal components of the strain and curvature are defined and computed in SI Appendix, section 3 and exhibit two

important features: 1) The lattice shears, $\epsilon_{12} = \epsilon_{21} = 0$, always vanish because the inner product $\ell_1 \cdot \ell_2$ depends only on the length of the edges and the interior angles of the faces and 2) the uniform face-bending mode exclusively generates twisting characterized by nonvanishing lattice curvatures, $\kappa_{12} = \kappa_{21}$, as previously observed for the special case of the Miura-ori (17, 18, 54). Together with the diagonal components, these quantities correspond to discrete analogs of the first and second fundamental forms (59) as discussed in *SI Appendix, section 4*. Since these are the only strains and curvatures permitted by linear isometries, any other mode of deformation requires stretching of the panels and, hence, requires significantly more energy. Consequently, we predict that in an origami sheet undergoing a nonuniform deformation due to loading conditions, any given unit cell would display some combination of the modes identified here (60, 61).

Poisson's Ratio Transitions. The Poisson's ratios in Eq. 25 change along the one-dimensional manifold of degenerate ground states; in particular, the Poisson's ratios can undergo transitions from positive to negative and vice versa as identified in the Morph family (20). Here, we show that such transitions occur whenever two adjacent faces are coplanar and determine the relationship between the intrinsic crease geometry and such ground states to reveal two subsets of four-parallel-gram origami that are strictly in-plane auxetic and strictly out-of-plane auxetic.

The Poisson's ratios change sign if and only if the ratio of global folding coefficients, χ_i , in Eq. 25 changes sign, which occurs when three of the edge vectors lie in the same plane. This corresponds to a ground state where two adjacent faces either lie flat to (Fig. 4 C, *Inset*) or lie on top of (Fig. 4 D, *Inset*) one another, which are respectively quantified by the dihedral angles between the faces: $\gamma_i = \pi$ or $\gamma_i = 0, 2\pi$. The spatial symmetry of the crease pattern implies that there are only four unique dihedral angles, as shown in Fig. 4A, and that those on parallel edges are complementary to one another, summing to 2π radians. Hence, the condition for the Poisson's ratios to change sign is determined by the existence of ground states for a single vertex with exactly one dihedral angle equal to an integer multiple of π .

The ground states of an origami vertex are the sets of dihedral angles compatible with the fixed sector angles, α_A (25, 26), labeled in Fig. 4A. The edges emanating from this vertex in a generic ground state project onto the unit sphere (*SI Appendix, Fig. S1C*), thereby mapping to the vertices of the spherical quadrilateral shown in Fig. 4B. This spherical quadrilateral has edges that are segments of great circles (geodesics of the sphere) with arc-length equal to the corresponding sector angles and interior angles that are equal to the corresponding dihedral angles. This mapping can be used to parameterize the ground states of a generic four-coordinated vertex via spherical trigonometry (25, 62) (*SI Appendix, section 1B*).

For the sake of determining the relationship between sector angles and Poisson's ratio transitions in four-parallel-gram origami, it suffices to determine the conditions for the "opened" configuration, $\gamma_1 = \pi$, shown in Fig. 4C, and the "closed" configuration, $\gamma_1 = 0$, shown in Fig. 4D. In both cases, the spherical quadrilateral flattens to a spherical triangle; hence, this dihedral angle, γ_1 , can take the value of π or 0 only when the respective spherical triangle inequalities are satisfied:

$$\|\alpha_A + \alpha_D\| \leq \|\alpha_B + \alpha_C\|, \quad [26]$$

$$\|\alpha_A - \alpha_D\| \geq \|\alpha_B - \alpha_C\|, \quad [27]$$

where the spherical norm, $\|x\| \equiv \min\{x, 2\pi - x\}$, takes the shortest of the two great circles connecting the vertices. Note that when one of the inequalities in Eqs. 26 and 27 is not satisfied, the corresponding inequality for γ_3 is satisfied.

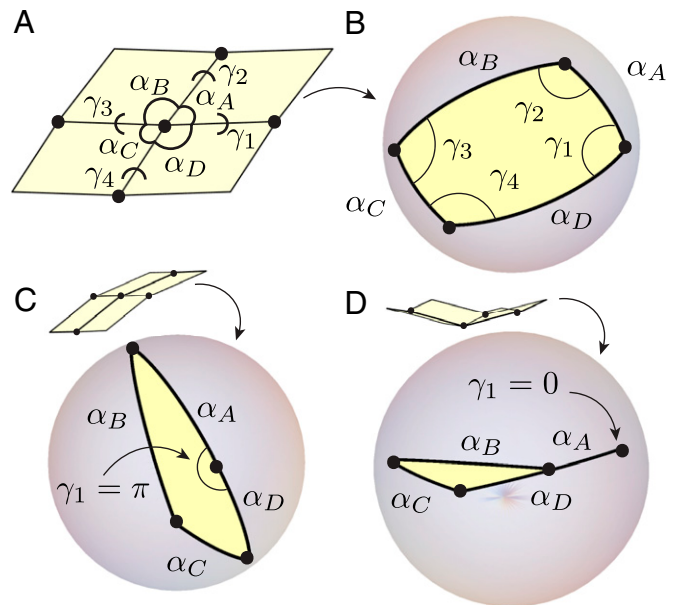


Fig. 4. (A) A generic four-coordinated vertex whose geometry is characterized by the sector angles, α , between subsequent edges and its ground state specified by the dihedral angles, γ , between adjacent faces. (B) The spherical quadrilateral obtained by projecting the edges in A onto the unit sphere. (C and D) "Opened" (C) ($\gamma_1 = \pi$) and "closed" (D) ($\gamma_1 = 0$) face configurations whose sector angles respectively satisfy Eqs. 26 and 27.

Generic choices of sector angles satisfy either one or both of the inequalities in Eqs. 26 and 27 for a particular crease. However, the constraints on the dihedral angles always possess two solutions (which are related by the inversion of the sheet $\gamma_i \rightarrow 2\pi - \gamma_i$) and these two cases correspond to different configuration space topologies (63). In the former, the two branches connect to satisfy the 2π periodicity of the constraints as shown in Fig. 5A. In the latter the two branches are disconnected because each branch is itself 2π periodic as shown in Fig. 5B. Note that this feature is independent of flattened configurations (57, 64) or curvature of the vertex (62). Nonetheless, both cases generically undergo Poisson's ratio transitions as shown in Fig. 5A and B, where it is important to note transitions at $\gamma_i = 0, 2\pi$ require self-intersection of the origami sheet and are hence nonphysical.

Special choices of sector angles that satisfy equality for both spherical inequalities have ground states for which the dihedral angles fold through 0 or π simultaneously. First, consider developable crease patterns, $\sum \alpha_A = 2\pi$, satisfying the Kawasaki condition for flat foldability (65), $\alpha_A + \alpha_C = \alpha_B + \alpha_D$, such as that shown in Fig. 5C. In this case, every dihedral angle folds through 0 or π simultaneously, thereby preventing the Poisson's ratio from changing sign. Second, consider crease patterns satisfying the generalized flat-foldable condition identified in ref. 46, $\alpha_A = \alpha_C, \alpha_B = \alpha_D$, such as that shown in Fig. 5D. In this case, nonadjacent dihedral angles fold through $\gamma_i = \gamma_{i+2} = 0$ or π simultaneously while the remaining two dihedral angles fold through $\gamma_{i+1} = \gamma_{i+3} = \pi$ or 0, respectively, thereby preventing the Poisson's ratio from changing sign. These two subsets of in-plane and out-of-plane negative Poisson's ratio origami metamaterials respectively reduce to the Miura-ori (17, 18) and eggbox (19) crease patterns.

Concluding Remarks

We have developed a framework for characterizing the low-energy deformations of quadrilateral-based origami sheets that enables

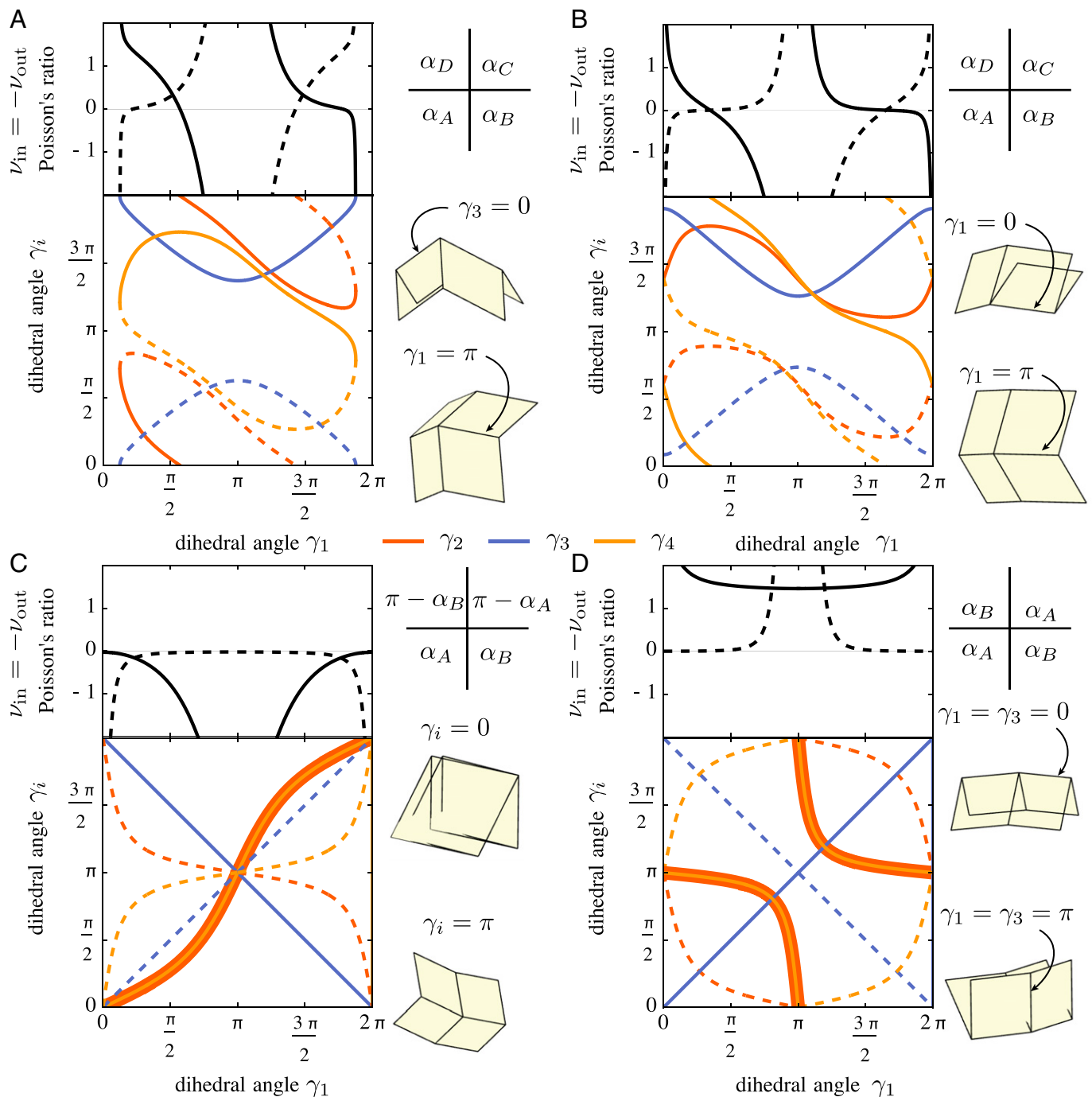


Fig. 5. (A–D) The Poisson's ratios, ν , and one-dimensional manifolds of degenerate ground states, $\gamma_i = \gamma_i(\gamma_1)$, for four-parallelgram origami sheets with (A) generic sector angles and connected solution branches, (B) generic sector angles and disconnected solution branches, (C) sector angles that ensure a strictly negative in-plane Poisson's ratio, and (D) sector angles that ensure a strictly positive in-plane Poisson's ratio. The Poisson's ratios change sign when exactly two of the faces are coplanar as indicated by a single dihedral angle folding through 0 or π . Note that these results, including the magnitude of the Poisson's ratios, are entirely independent of the overall length scale of the sheet.

investigations of the interplay between discrete symmetries and mechanical response. We have implemented this formalism for periodic crease patterns with unit cells composed of four generic parallelogram faces, thereby revealing that in such sheets the infinitesimal strains are induced by a symmetric mode whereas the infinitesimal curvatures are induced by an antisymmetric mode. Moreover, we have showed that these quantities define geometric Poisson's ratios that are always equal and opposite to one another, contrasting the relationship found in conventional elasticity. Finally, we have discovered subsets within this family of crease patterns that have strictly negative in-plane or

out-of-plane Poisson's ratios that may be utilized as auxetic mechanical metamaterials.

The formalism developed herein extends to the analysis of crease patterns beyond four-parallelgram origami. The compatibility conditions can be immediately applied to determine the linear isometries in parallelogram-based origami with larger unit cells (66, 67) as well as Bloch-periodic modes (54, 57). Furthermore, the symmetry analysis of these compatibility conditions could be used to constrain the stiffness of parallel-based origami tubes (51, 68). Finally, the compatibility conditions can also be used to explore the role of discrete symmetries in crease patterns with more

generic quadrilateral faces where the face amplitudes cannot be integrated out of the linear constraints (45–49).

The experimental realization of these structures requires a number of important considerations. The work in the present article considers only the uniform geometry of the origami sheets whereas the elastic properties of physical materials can favor one mode of deformation over the others (52, 53, 69) and imperfections can significantly alter the mechanical response (70, 71). Moreover, local actuation typically leads to nonuniform deformations (72–74) and creases tend to exhibit temporal relaxation dynamics (75) that give rise to plastic memory effects (76). Thus, it remains to explore the ability to control the mechanical response of physical origami via this geometric symmetry.

In conclusion, the symmetry analysis of linear isometries provides a systematic characterization of the large-scale deformations in parallelogram-based origami. More generally, similar analysis can be applied to systems where symmetries constrain both the intracellular and intercellular properties, which may be insightful

for the design of metamaterials in mechanics (77–81) and beyond (82, 83).

Data Availability. There are no data underlying this work.

Note Added in Proof. While this article was under review, calculations for the in-plane Poisson's ratio of the Morph subfamily were experimentally verified in ref. 84 and the equal-and-opposite property of generic four-parallelogram origami sheets was computed via an alternative calculation in ref. 85.

ACKNOWLEDGMENTS. We thank Michael Czajkowski for helpful discussions and Christian D. Santangelo for feedback on the manuscript.

Author affiliations: ^aSchool of Physics, Georgia Institute of Technology, Atlanta, GA 30332; ^bDepartment of Physics, University of Michigan, Ann Arbor, MI 48109; ^cSchool of Civil Engineering, Georgia Institute of Technology, Atlanta, GA 30332; ^dDepartment of Civil and Environmental Engineering, Princeton University, Princeton, NJ 08544; ^ePrinceton Institute for the Science and Technology of Materials, Princeton University, Princeton, NJ 08544; and ^fDepartment of Mechanical and Aerospace Engineering, Princeton University, Princeton, NJ 08544

1. H. Weyl, *The Theory of Groups and Quantum Mechanics* (Courier Corporation, 1950).
2. M. S. Dresselhaus, G. Dresselhaus, A. Jorio, *Group Theory: Application to the Physics of Condensed Matter* (Springer Science & Business Media, 2007).
3. A. Altland, M. R. Zirnbauer, Nonstandard symmetry classes in mesoscopic normal-superconducting hybrid structures. *Phys. Rev. B Condens. Matter* **55**, 1142 (1997).
4. A. P. Schnyder, S. Ryu, A. Furusaki, A. W. Ludwig, Classification of topological insulators and superconductors in three spatial dimensions. *Phys. Rev. B Condens. Matter Mater. Phys.* **78**, 195125 (2008).
5. A. Kitaev, "Periodic table for topological insulators and superconductors" in *AIP Conference Proceedings*, V. Lebedev, M. Feigel'ma, Eds. (American Institute of Physics, College Park, MD, 2009), vol. 1134, pp. 22–30.
6. S. Ryu, A. P. Schnyder, A. Furusaki, A. W. Ludwig, Topological insulators and superconductors: Tenfold way and dimensional hierarchy. *New J. Phys.* **12**, 065010 (2010).
7. K. Roychowdhury, M. J. Lawler, Classification of magnetic frustration and metamaterials from topology. *Phys. Rev. B* **98**, 094432 (2018).
8. R. Süsstrunk, S. D. Huber, Classification of topological phonons in linear mechanical metamaterials. *Proc. Natl. Acad. Sci. U.S.A.* **113**, E4767–E4775 (2016).
9. S. D. Guest, P. W. Fowler, Symmetry-extended counting rules for periodic frameworks. *Philos. Trans. R. Soc. A Math. Phys. Eng. Sci.* **372**, 20120029 (2013).
10. H. Mitschke, G. Schröder-Turk, K. Mecke, P. Fowler, S. Guest, Symmetry detection of auxetic behaviour in 2d frameworks. *Europhys. Lett.* **102**, 66005 (2013).
11. P. W. Fowler, S. D. Guest, T. Tarnai, Symmetry perspectives on some auxetic body-bar frameworks. *Symmetry (Basel)* **6**, 368–382 (2014).
12. S. Babaei et al., 3D soft metamaterials with negative Poisson's ratio. *Adv. Mater.* **25**, 5044–5049 (2013).
13. X. Hou, V. V. Silberschmidt, "Metamaterials with negative Poisson's ratio: A review of mechanical properties and deformation mechanisms" in *Mechanics of Advanced Materials*, V. V. Silberschmidt, V. P. Matveenko, Eds. (Springer International Publishing, 2015), pp. 155–179.
14. H. M. Kolken, A. Zadpoor, Auxetic mechanical metamaterials. *RSC Advances* **7**, 5111–5129 (2017).
15. P. U. Kelkar et al., Cellular auxetic structures for mechanical metamaterials: A review. *Sensors (Basel)* **20**, 3132 (2020).
16. L. D. Landau, E. M. Lifshitz, *Course of Theoretical Physics: Theory and Elasticity* (Pergamon Press, 1959), vol. 7.
17. Z. Y. Wei, Z. V. Guo, L. Dudte, H. Y. Liang, L. Mahadevan, Geometric mechanics of periodic pleated origami. *Phys. Rev. Lett.* **110**, 215501 (2013).
18. M. Schenk, S. D. Guest, Geometry of Miura-folded metamaterials. *Proc. Natl. Acad. Sci. U.S.A.* **110**, 3276–3281 (2013).
19. H. Nassar, A. Lebée, L. Monasse, Curvature, metric and parametrization of origami tessellations: Theory and application to the eggbox pattern. *Proc. R. Soc. A Math. Phys. Eng. Sci.* **473**, 20160705 (2017).
20. P. P. Pratapa, K. Liu, G. H. Paulino, Geometric mechanics of origami patterns exhibiting Poisson's ratio switch by breaking mountain and valley assignment. *Phys. Rev. Lett.* **122**, 155501 (2019).
21. E. A. Peraza-Hernandez, D. J. Hartl, R. J. Malak Jr., D. C. Lagoudas, Origami-inspired active structures: A synthesis and review. *Smart Mater. Struct.* **23**, 094001 (2014).
22. J. Rogers, Y. Huang, O. G. Schmidt, D. H. Gracias, Origami mems and nems. *MRS Bull.* **41**, 123–129 (2016).
23. C. D. Santangelo, Extreme mechanics: Self-folding origami. *Annu. Rev. Condens. Matter Phys.* **8**, 165–183 (2017).
24. C. D. Santangelo, Theory and practice of origami in science. *Soft Matter* **16**, 94–101 (2020).
25. D. A. Huffman, Curvature and creases: A primer on paper. *IEEE Trans. Comput.* **25**, 1010–1019 (1976).
26. S.-M. Belcastro, T. C. Hull, Modelling the folding of paper into three dimensions using affine transformations. *Linear Algebra Appl.* **348**, 273–282 (2002).
27. E. Hawkes et al., Programmable matter by folding. *Proc. Natl. Acad. Sci. U.S.A.* **107**, 12441–12445 (2010).
28. M. T. Tolley et al., Self-folding origami: Shape memory composites activated by uniform heating. *Smart Mater. Struct.* **23**, 094006 (2014).
29. D. Melancon, B. Gorissen, C. J. Garcia-Mora, C. Hoberman, K. Bertoldi, Multistable inflatable origami structures at the metre scale. *Nature* **592**, 545–550 (2021).
30. N. Bassik, G. M. Stern, D. H. Gracias, Microassembly based on hands free origami with bidirectional curvature. *Appl. Phys. Lett.* **95**, 91901 (2009).
31. J. H. Cho et al., Nanoscale origami for 3D optics. *Small* **7**, 1943–1948 (2011).
32. N. Lazarus, G. L. Smith, M. D. Dickey, Self-folding metal origami. *Adv. Intell. Syst.* **1**, 1900059 (2019).
33. Y. Liu, J. K. Boyles, J. Genzer, M. D. Dickey, Self-folding of polymer sheets using local light absorption. *Soft Matter* **8**, 1764–1769 (2012).
34. J. H. Na et al., Programming reversibly self-folding origami with micropatterned photo-crosslinkable polymer trilayers. *Adv. Mater.* **27**, 79–85 (2015).
35. Y. Liu, J. Genzer, M. D. Dickey, "2d or not 2d": Shape-programming polymer sheets. *Prog. Polym. Sci.* **52**, 79–106 (2016).
36. Y. Liu, B. Shaw, M. D. Dickey, J. Genzer, Sequential self-folding of polymer sheets. *Sci. Adv.* **3**, e1602417 (2017).
37. Z. Lin et al., Folding at the microscale: Enabling multifunctional 3d origami-architected metamaterials. *Small* **16**, e2002229 (2020).
38. M. Z. Miskin et al., Graphene-based bimorphs for micron-sized, autonomous origami machines. *Proc. Natl. Acad. Sci. U.S.A.* **115**, 466–470 (2018).
39. N. Turner, B. Goodwine, M. Sen, A review of origami applications in mechanical engineering. *Proc. Inst. Mech. Eng. C J. Mech. Eng. Sci.* **230**, 2345–2362 (2016).
40. M. Meloni et al., Engineering origami: A comprehensive review of recent applications, design methods, and tools. *Adv. Sci.* **8**, 2000636 (2021).
41. S. J. Kim, D. Y. Lee, G. P. Jung, K. J. Cho, An origami-inspired, self-locking robotic arm that can be folded flat. *Sci. Robot.* **3**, eaar2915 (2018).
42. W. Kim et al., Bioinspired dual-morphing stretchable origami. *Sci. Robot.* **4**, eaay3493 (2019).
43. L. S. Novellino, Q. Ze, S. Wu, G. H. Paulino, R. Zhao, Untethered control of functional origami microrobots with distributed actuation. *Proc. Natl. Acad. Sci. U.S.A.* **117**, 24096–24101 (2020).
44. S. Wu et al., Stretchable origami robotic arm with omnidirectional bending and twisting. *Proc. Natl. Acad. Sci. U.S.A.* **118**, e2110023118 (2021).
45. T. Tachi, Generalization of rigid-foldable quadrilateral-mesh origami. *J. Int. Assoc. Shell Spat. Struct.* **50**, 173–179 (2009).
46. S. Waitukaitis, R. Menaut, B. G. Chen, M. van Hecke, Origami multistability: From single vertices to metasheets. *Phys. Rev. Lett.* **114**, 055503 (2015).
47. T. A. Evans, R. J. Lang, S. P. Magleby, L. L. Howell, Rigidly foldable origami gadgets and tessellations. *R. Soc. Open Sci.* **2**, 150067 (2015).
48. F. Feng, X. Dang, R. D. James, P. Plucinsky, The designs and deformations of rigidly and flat-foldable quadrilateral mesh origami. *J. Mech. Phys. Solids* **142**, 104018 (2020).
49. P. Dieleman, N. Vasmel, S. Waitukaitis, M. van Hecke, Jigsaw puzzle design of pluripotent origami. *Nat. Phys.* **16**, 63–68 (2020).
50. C. Lv, D. Krishnaraju, G. Konjevod, H. Yu, H. Jiang, Origami based mechanical metamaterials. *Sci. Rep.* **4**, 5979 (2014).
51. E. T. Filipov, T. Tachi, G. H. Paulino, Origami tubes assembled into stiff, yet reconfigurable structures and metamaterials. *Proc. Natl. Acad. Sci. U.S.A.* **112**, 12321–12326 (2015).
52. M. Schenk, S. D. Guest, "Origami folding: A structural engineering approach" in *SOSME, 5th International Conference on Origami in Science, Mathematics and Education*, P. Wang-Iverson, R. J. Lang, M. Yim, Eds. (CRC Press, Boca Raton, FL, 2010).
53. E. Filipov, K. Liu, T. Tachi, M. Schenk, G. H. Paulino, Bar and hinge models for scalable analysis of origami. *Int. J. Solids Struct.* **124**, 26–45 (2017).
54. A. A. Evans, J. L. Silverberg, C. D. Santangelo, Lattice mechanics of origami tessellations. *Phys. Rev. E Stat. Nonlin. Soft Matter Phys.* **92**, 013205 (2015).
55. H. Gluck, "Almost all simply connected closed surfaces are rigid" in *Geometric Topology*, L. C. Glaser, T. B. Rushing, Eds. (Springer, 1975), pp. 225–239.
56. H. Crapo, W. Whiteley, Statics of frameworks and motions of panel structures: A projective geometric introduction. *Struct. Topol.* **1982**, 6 (1982).
57. J. McInerney, B. G. Chen, L. Theran, C. D. Santangelo, D. Z. Rocklin, Hidden symmetries generate rigid folding mechanisms in periodic origami. *Proc. Natl. Acad. Sci. U.S.A.* **117**, 30252–30259 (2020).
58. T. Ting, T. Chen, Poisson's ratio for anisotropic elastic materials can have no bounds. *Q. J. Mech. Appl. Math.* **58**, 73–82 (2005).
59. D. Lovelock, H. Rund, *Tensors, Differential Forms, and Variational Principles* (Courier Corporation, 1989).
60. M. Czajkowski, C. Coulais, M. van Hecke, D. Z. Rocklin, Conformal elasticity of mechanism-based metamaterials. *Nat. Commun.* **13**, 211 (2022).

61. Y. Zheng, I. Niloy, P. Celli, I. Tobasco, P. Plucinsky, Continuum field theory for the deformations of planar kirigami. *Phys. Rev. Lett.* **128**, 208003 (2022).
62. M. Berry, M. E. Lee-Trimble, C. D. Santangelo, Topological transitions in the configuration space of non-Euclidean origami. *Phys. Rev. E* **101**, 043003 (2020).
63. C. Chiang, On the classification of spherical four-bar linkages. *Mech. Mach. Theory* **19**, 283-287 (1984).
64. B. G. Chen, C. D. Santangelo, Branches of triangulated origami near the unfolded state. *Phys. Rev. X* **8**, 011034 (2018).
65. J. O'Rourke, *How to Fold It: The Mathematics of Linkages, Origami, and Polyhedra* (Cambridge University Press, 2011).
66. Y. Klett, "Realtime rigid folding algorithm for quadrilateral-based 1-dof tessellations" in *International Design Engineering Technical Conferences and Computers and Information in Engineering Conference* (American Society of Mechanical Engineers, New York, NY, 2013), vol. 55942, p. V06BT07A031.
67. X. Zhou, S. Zang, Z. You, Origami mechanical metamaterials based on the Miura-derivative fold patterns. *Proc. R. Soc. A Math. Phys. Eng. Sci.* **472**, 20160361 (2016).
68. J. T. Overvelde *et al.*, A three-dimensional actuated origami-inspired transformable metamaterial with multiple degrees of freedom. *Nat. Commun.* **7**, 10929 (2016).
69. K. Liu, G. H. Paulino, Nonlinear mechanics of non-rigid origami: An efficient computational approach. *Proc. Math. Phys. Eng. Sci.* **473**, 20170348 (2017).
70. M. B. Pinson *et al.*, Self-folding origami at any energy scale. *Nat. Commun.* **8**, 15477 (2017).
71. K. Liu, L. S. Novelino, P. Gardoni, G. H. Paulino, Big influence of small random imperfections in origami-based metamaterials. *Proc. R. Soc. A* **476**, 20200236 (2020).
72. M. Stern, M. B. Pinson, A. Murugan, The complexity of folding self-folding origami. *Phys. Rev. X* **7**, 041070 (2017).
73. S. Grey, M. Schenk, F. Scarpa, "Local actuation of tubular origami" in *Proceedings of the Seventh Meeting of Origami, Science, Mathematics and Education, Oxford, UK*, R. J. Lang, M. Bolitho, Z. You, Eds. (Tarquin Publications, St. Albans, United Kingdom, 2018), pp. 4-7.
74. S. W. Grey, F. Scarpa, M. Schenk, Strain reversal in actuated origami structures. *Phys. Rev. Lett.* **123**, 025501 (2019).
75. B. Thiria, M. Adda-Bedia, Relaxation mechanisms in the unfolding of thin sheets. *Phys. Rev. Lett.* **107**, 025506 (2011).
76. T. Jules, F. Lechenault, M. Adda-Bedia, Plasticity and aging of folded elastic sheets. *Phys. Rev. E* **102**, 033005 (2020).
77. A. A. Zadpoor, Mechanical meta-materials. *Mater. Horiz.* **3**, 371-381 (2016).
78. K. Bertoldi, V. Vitelli, J. Christensen, M. Van Hecke, Flexible mechanical metamaterials. *Nat. Rev. Mater.* **2**, 1-11 (2017).
79. X. Yu, J. Zhou, H. Liang, Z. Jiang, L. Wu, Mechanical metamaterials associated with stiffness, rigidity and compressibility: A brief review. *Prog. Mater. Sci.* **94**, 114-173 (2018).
80. E. Barchiesi, M. Spagnuolo, L. Placidi, Mechanical metamaterials: A state of the art. *Math. Mech. Solids* **24**, 212-234 (2019).
81. J. U. Surjadi *et al.*, Mechanical metamaterials and their engineering applications. *Adv. Eng. Mater.* **21**, 1800864 (2019).
82. M. Wegener, Materials science. Metamaterials beyond optics. *Science* **342**, 939-940 (2013).
83. M. Kadic, T. Bückmann, R. Schittny, M. Wegener, Metamaterials beyond electromagnetism. *Rep. Prog. Phys.* **76**, 126501 (2013).
84. D. Misseroni, P. P. Pratapa, K. Liu, G. H. Paulino, Experimental realization of tunable Poisson's ratio in deployable origami metamaterials. *Extreme Mech. Lett.* **53**, 101685 (2022).
85. H. Nassar, A. Lebé, E. Werner, Strain compatibility and gradient elasticity in morphing origami metamaterials. *Extreme Mech. Lett.* **53**, 101722 (2022).